PNAS Nexus, 2023, 2, 1–8
https://doi.org/10.1093/pnasnexus/pgad268
Advance access publication 14 August 2023
Research Report

Molecular basis for inhibition of methane clathrate growth by a deep subsurface bacterial protein

Dustin J. E. Huard [a,1], Abigail M. Johnson [b,1,2], Zixing Fan [c], Lydia G. Kenney [a], Manlin Xu [b,3], Ran Drori [d], James C. Gumbart [a,e], Sheng Dai [f], Raquel L. Lieberman [a] and Jennifer B. Glass [b,*]

[a]School of Chemistry and Biochemistry, Georgia Institute of Technology, 901 Atlantic Drive NW, Atlanta, GA 30332, USA
[b]School of Earth and Atmospheric Sciences, Georgia Institute of Technology, 311 Ferst Drive NW, Atlanta, GA 30332, USA
[c]Interdisciplinary Bioengineering Graduate Program, Georgia Institute of Technology, 315 Ferst Dr NW, Atlanta, GA 30332, USA
[d]Department of Chemistry and Biochemistry, Yeshiva University, 245 Lexington Ave Room 548, New York, NY 10016, USA
[e]School of Physics, Georgia Institute of Technology, 837 State Street, Atlanta, GA 30332, USA
[f]School of Civil and Environmental Engineering, Georgia Institute of Technology, 790 Atlantic Drive NW, Atlanta, GA 30332, USA
*To whom correspondence should be addressed: Email: jennifer.glass@eas.gatech.edu
[1]D.J.E.H. and A.M.J. contributed equally to this work.
[2]Present address: Department of Marine Sciences, University of Georgia, Athens, GA, USA.
[3]Present address: Department of Earth, Environmental and Planetary Sciences, Brown University, Providence, RI, USA.
Edited By: Cristina Amon

Abstract

Methane clathrates on continental margins contain the largest stores of hydrocarbons on Earth, yet the role of biomolecules in clathrate formation and stability remains almost completely unknown. Here, we report new methane clathrate-binding proteins (CbpAs) of bacterial origin discovered in metagenomes from gas clathrate-bearing ocean sediments. CbpAs show similar suppression of methane clathrate growth as the commercial gas clathrate inhibitor polyvinylpyrrolidone and inhibit clathrate growth at lower concentrations than antifreeze proteins (AFPs) previously tested. Unlike AFPs, CbpAs are selective for clathrate over ice. $CbpA_3$ adopts a nonglobular, extended structure with an exposed hydrophobic surface, and, unexpectedly, its TxxxAxxxAxx motif common to AFPs is buried and not involved in clathrate binding. Instead, simulations and mutagenesis suggest a bipartite interaction of CbpAs with methane clathrate, with the pyrrolidine ring of a highly conserved proline residue mediating binding by filling empty clathrate cages. The discovery that CbpAs exert such potent control on methane clathrate properties implies that biomolecules from native sediment bacteria may be important for clathrate stability and habitability.

Keywords: methane clathrate, protein structure, ocean sediment, subsurface bacteria, molecular simulations

Significance Statement

We report a bacterial protein native to marine sediments that inhibits the growth of methane clathrate via a previously unknown mechanism. These novel clathrate-binding proteins are completely different in structure and inhibitory mechanism from known antifreeze proteins and are selective for clathrate over ice. This study provides a new window into biological controls on previously unconsidered methane clathrate stability and habitability in nature.

Introduction

Methane clathrates, cages of water that trap methane gas, store thousands of gigatons of carbon on Earth's continental shelves and in permafrost deposits (1–4), and may harbor habitable environments for life on other planetary bodies (5). Clathrates contain unique microbial communities that are adapted for life at low temperature, high salinity, and high pressure (6). Because clathrate formation during deep-water drilling operations poses serious hazards (7, 8), chemical clathrate inhibitors are commonly added to drilling fluids at high concentrations to suppress clathrate formation (9, 10). Thermodynamic clathrate inhibitors such as ethanol and methanol are used commercially to reduce clathrate formation temperature but require large doses due to the fast water flow rates required (11). Kinetic clathrate inhibitors, such as the polymers polyvinylpyrrolidone (PVP) and polyvinyl caprolactam, delay clathrate nucleation and crystal growth and require lower doses with slower flow rates needed (11, 12); such water-soluble polymers are nonbiodegradable and accumulate in the environment (13). The ongoing search for eco-friendly gas clathrate inhibitors motivated studies of the response of gas clathrate growth to the presence of antifreeze proteins (AFPs) from various cold-dwelling organisms (14). Type I AFPs isolated from

Competing Interest: The authors declare no competing interest.
Received: May 23, 2023. **Revised:** July 25, 2023. **Accepted:** August 10, 2023

cold-water fish have been shown to be gas clathrate inhibitors (15) but are not scalable for industrial application (14).

In this study, we report bacterial clathrate-binding proteins (CbpAs) that potently inhibit methane clathrate growth. These bacterial CbpAs were initially discovered in metagenomes from deep subsurface methane clathrate-bearing sediments based on their threonine-alanine (TxxxAxxxAxx) motifs common to AFPs (16). Recombinantly expressed and purified CbpAs bind to and alter the morphology of structure II tetrahydrofuran clathrate, a low-pressure analog for gas clathrate (16). Here, we show that these proteins suppress methane clathrate growth and we then provide a molecular basis for this activity through structural and biochemical studies combined with molecular dynamic (MD) simulations. The discovery of CbpAs indicates that native sediment bacteria possess such biomolecules for clathrate stability and habitability, and provides a path forward for a scalable, eco-friendly industrial gas clathrate inhibitor.

Results

Activity toward methane clathrate

Having previously determined that CbpAs are capable of modifying structure II clathrate and inhibiting its growth, we sought to ascertain whether CbpAs interact with biologically relevant structure I methane clathrate in which their originators dwell. Of the CbpA homologs tested, $CbpA_3$ was the most potent inhibitor of methane clathrate growth. Compared with the buffer-only control, treatments with $CbpA_3$ grew significantly less methane clathrate ($P = 0.003$; Fig. 1A), and clathrate dissociated at significantly higher pressure ($P = 0.01$; Fig. 1A and B). Clathrate dissociation also occurred more quickly in treatments with CbpAs due to less clathrate being formed (Fig. S1). Equimolar $CbpA_3$ and PVP treatments were not significantly different in gas consumption ($P = 1.00$; Fig. 1A) nor in dissociation pressure ($P = 0.99$; Fig. 1A and B). Other CbpAs tested, namely $CbpA_2$, $CbpA_5$, and $CbpA_6$, suppressed clathrate growth and elevated dissociation pressure, but with more variability than PVP or $CbpA_3$ (Fig. 1A and B). Clathrate growth and stability in phosphate-buffered saline (PBS) buffer were unaffected by cytochrome *c* ($P = 0.97$; $P = 0.90$) or type I AFP ($P = 0.27$; $P = 0.91$; Fig. 1A and B). Our results for type I AFP are consistent with analogous assays in a different experimental setup (18). Unlike type I AFPs (18, 19), all CbpAs tested ($CbpA_3$, $CbpA_5$, and $CbpA_6$) do not bind to ice and have no effect on ice growth (Movie S1 and Fig. S2). Notably, all CbpAs were more active inhibitors of clathrate growth at lower concentrations than previously tested AFPs (Fig. 2).

Morphological differences are apparent in clathrate shells generated from different samples in our custom pressure cell. Droplets containing CbpAs or PVP that inhibit clathrate formation generate smooth and rounded clathrate shells (Fig. 3). In contrast, clathrate formed by droplets with buffer, cytochrome *c*, or type I AFP appears as cratered domes, with depressions in the center of the droplets. At low driving forces, where the difference between the Gibbs free energy of the solution and the crystal phases is relatively small, cratering in clathrate shells commonly occurs over long periods of time (≥24 h) near stability boundaries (29–31). The high driving forces during clathrate nucleation (−9°C and 5 MPa) in our experiments likely result in rapid growth in the absence of inhibitors, causing water to be pulled from the center to the sides for further clathrate formation (Fig. 3), as observed at high driving forces in a previous study (32).

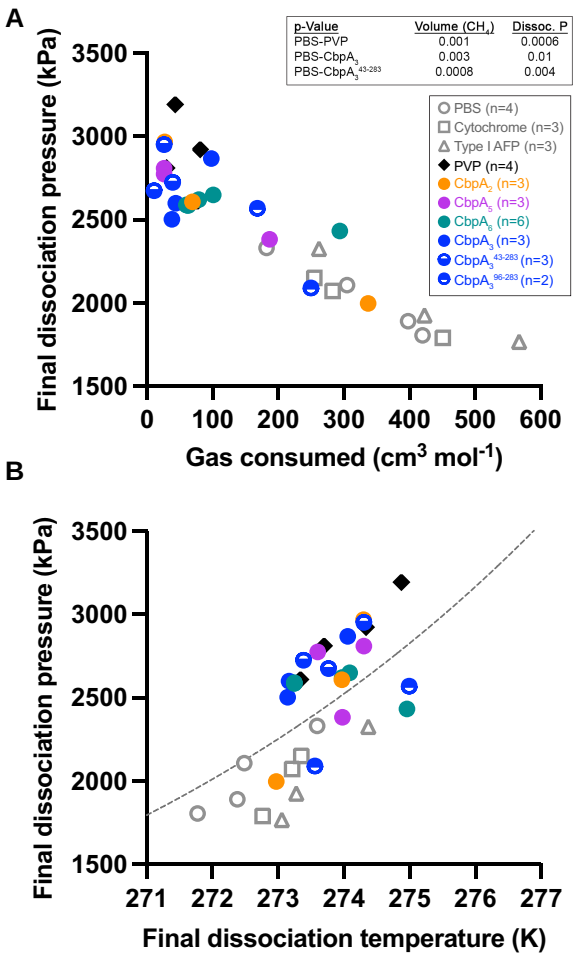

Fig. 1. Effect of CbpAs on clathrate growth and stability. A) Greater volume of gas consumed is indicative of more clathrate growth, and greater final dissociation pressure is indicative of less stable clathrate. The inset shows significant *P*-values from Student's *t* tests of the buffer solution (PBS) with pairs for gas consumed (Volume(CH_4)) and final dissociation pressure (Dissoc. P). B) Clathrate stability is measured by final clathrate dissociation temperature and pressure. The dotted gray line: clathrate stability curve from Sloan and Koh (17,).

Structure determination of $CbpA_3$

To clarify the molecular basis of methane clathrate inhibition, we conducted crystallization trials of CbpAs. After extensive testing of various parameters such as protein identity, protein buffer, protein concentration, limited proteolysis, and sparse matrix conditions, promising hits were obtained for $CbpA_3$. Mass spectrometry analysis of $CbpA_3$ crystals similar to those ultimately used for structure determination confirmed that $CbpA_3$ was truncated in situ to residues 43–283. Subsequently, pretreatment of $CbpA_3$ with actinase E yielded crystals suitable for structure determination (Fig. S3).

We obtained phases for $CbpA_3$ crystal diffraction data by molecular replacement. The search model was the highest confidence region (56 residues) of the AlphaFold2 (33) model generated with ColabFold (34). Outside of these 56 residues, the AlphaFold-predicted structure is of very low confidence (not shown). The refined 3 Å resolution experimental model comprises residues 99–268 and encompasses the only TxxxAxxxAxx sequence motif in $CbpA_3$ (Fig. S4). The root-mean-square deviation (rmsd) between the initial 56 residue model used for phasing and the corresponding residues in the final experimental

structure is 0.5 Å. In contrast, the rmsd between the 170-residue final experimental structure and the full predicted AlphaFold model is 4.9 Å (not shown). Thus, despite serving a critical role in obtaining phases for our experimental structure, additional detailed insights are not possible from the low-confidence AlphaFold model. Finally, we infer that susceptibility to proteolysis leading to a structurally characterized fragment likely derives from linker regions flanking the crystallized fragment. The contribution of N- and C-terminal regions of $CbpA_3$ to clathrate inhibition will be the focus of future studies.

Constructs corresponding to identified proteolytic fragments of $CbpA_3$, namely $CbpA_3^{43–283}$ from mass spectrometry and $CbpA_3^{96–283}$ slightly larger than the observed structure, inhibited methane clathrate growth (Figs. 1A and 2) and increased dissociation pressure (Fig. 1A and B), confirming the relevance of these constructs to methane clathrate inhibition by $CbpA_3$. Inhibition by $CbpA_3^{43–283}$ was particularly robust ($P = 0.0008$; Figs. 1A, B and 2) compared with buffer-only control. $CbpA_3^{96–283}$, which was assayed at a lower concentration due to lower protein yield from purification, exhibited a moderate, but detectable, inhibitory effect (Figs. 1A, B and 2). Taken together, the structure of $CbpA_3^{99–268}$ provides a critical starting point for comprehending how these proteins function at a molecular level.

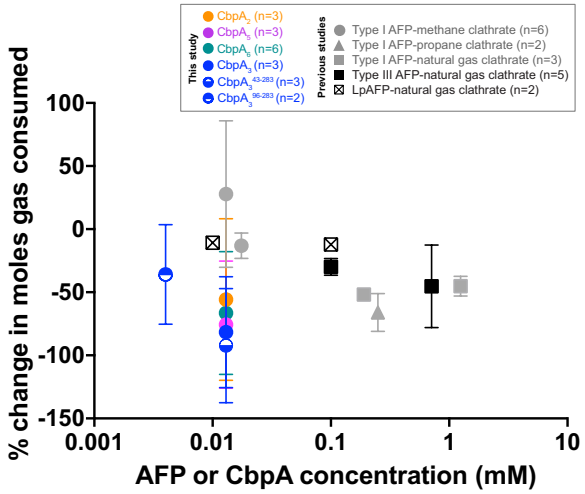

Fig. 2. Effects of AFPs and CbpAs on clathrate growth compared with control. Clathrate growth is measured by percent change in gas consumed relative to the control; the more negative values indicate less clathrate growth. Data for type I AFP (gray), type III AFP (black), and *Lp*AFP (*Lolium perenne*; perennial rye grass) AFP (cross) tested on natural gas clathrate (squares), methane clathrate (circles), and propane clathrates (triangles) were compiled from the literature (20–28); see Table S1 for experimental conditions in previous studies. The colored circles show the mean % change for CbpAs tested on methane clathrate in this study. The error bars represent ±1 SEM.

$CbpA_3$ structure

The structure of $CbpA_3^{99–268}$ (PDB 8DOT) reveals a largely α-helical and unprecedented nonglobular protein (Fig. 4A and Table S2) with two surprising features. First, the TxxxAxxxAxx motif, which was used to identify $CbpA_3$ as a CbpA candidate (16), is buried at the interface of two α-helices (Fig. 4B). Based on precedents from AFPs (35), these Thr and Ala residues were expected to be surface exposed for activity against gas clathrate, as they are believed to insert into partially formed clathrate cages at the growing clathrate surface in a manner similar to methane guest molecules. Second, $CbpA_3$ contains an unusual surface-exposed hydrophobic

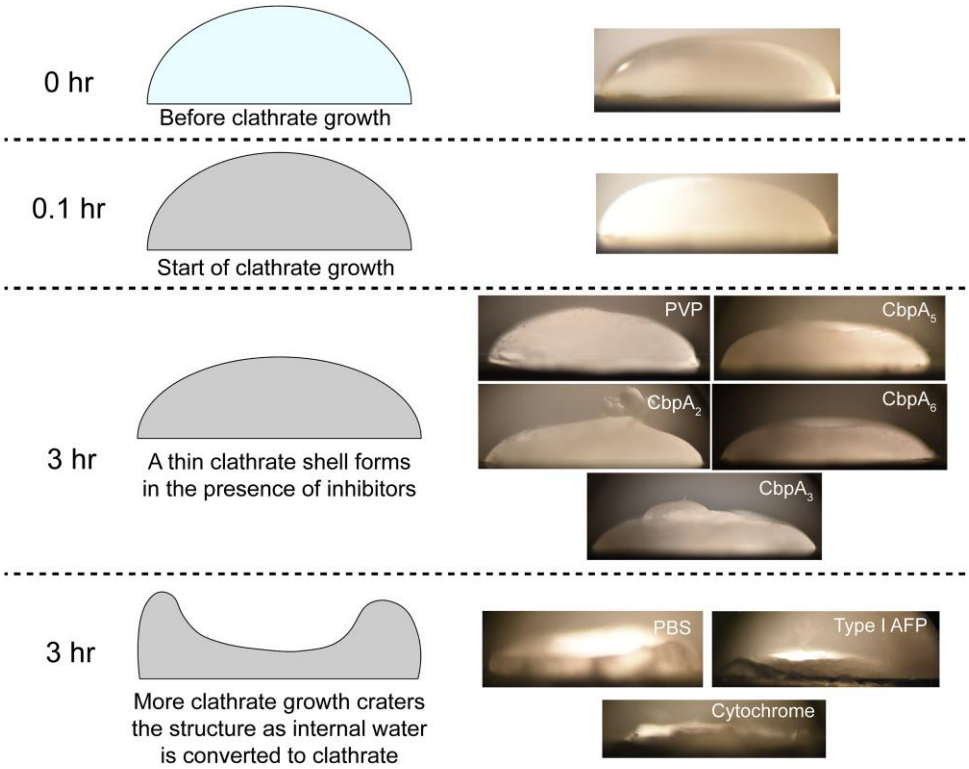

Fig. 3. Morphological impact of inhibitors on methane clathrate shell. Left: a cartoon illustrating methane clathrate development at the beginning of clathrate growth and at 3 h, with and without inhibitors. Right: representative photographs of experimental methane clathrate of each growth stage, labeled by treatment.

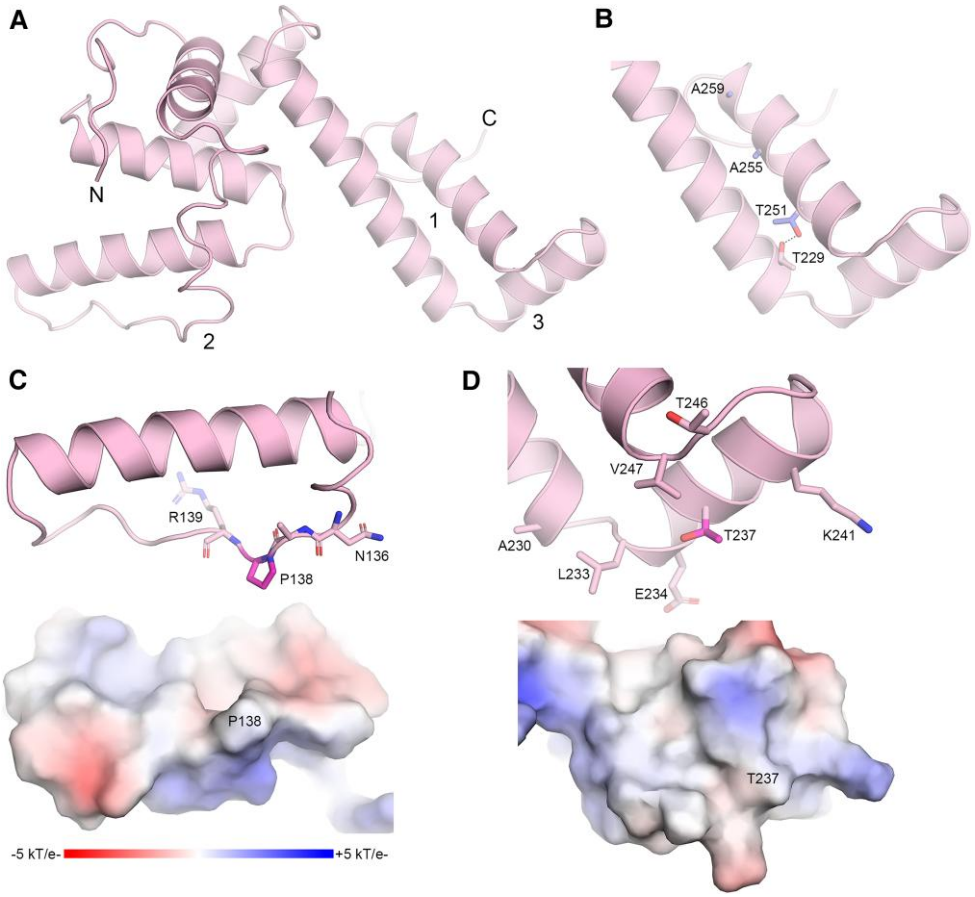

Fig. 4. Overall architecture and key structural features of $CbpA_3^{99–268}$. A) Cartoon representation of $CbpA_3^{99–268}$ with N- and C-termini labeled. Key structural elements are indicated by 1–3, which are detailed in panels B–D, respectively. B) Sole TxxxAxxxAxx motif of $CbpA_3$. Motif residues colored blue and shown as sticks. The dashed line represents hydrogen bond (3.3 Å) between Thr side chains on opposing helices. C) Top, cartoon representation of the clathrate-binding loop harboring P138 (magenta sticks). Bottom, electrostatic surface potential of the clathrate-binding loop, colored negative (red, −5 kT/e−) to positive (blue, +5 kT/e−). D) Cartoon (top) and electrostatic surface potential (bottom) views of clathrate-interacting helix containing T237 (magenta sticks). Electrostatic surface potential colored as in C).

patch (Fig. S5); inside a cleft in this feature, the structure contains a polyethylene glycol molecule. Except for Trp235, the residues comprising this hydrophobic surface are largely conserved across putative CbpA homologs (Table S3 and Fig. S6).

MD simulations

Having established that the components of $CbpA_3^{99–268}$ visible in our structure reflect a protein that inhibits methane clathrate, we next performed MD simulations to gain mechanistic insight into regions of this portion of the protein that are critical for methane clathrate binding. Starting from two replicas of six distinct orientations of the protein 25 Å from the clathrate surface, spontaneous sustained binding was observed in three of the twelve 1-μs simulations. These binding events revealed two potential interaction sites on the protein (Fig. 5A and B, Movies S2 and S3). The first site, centered on Pro138 located on a flat, nonpolar loop (Fig. 4C), was the most consistent interface identified, and binding occurred via the pyrrolidine ring of Pro138 filling an empty clathrate cage (Fig. 5A and B). The second surface is anchored by Thr237 (Fig. 4D) and is also flat and relatively uncharged. The most stable in silico interaction involved bipartite binding through both Pro138 and Thr237 sites (Fig. 5A). None of the simulations yielded interactions involving the TxxxAxxxAxx motif, which remained buried.

To determine the favorability of the observed binding interactions, we estimated the binding free energies with enhanced sampling calculations. Starting from the most stable binding pose (Fig. 5A), we defined a collective variable as a reaction coordinate for each binding site, namely the distance between Pro138 and the clathrate surface as well as that between Thr237 and the surface. To determine the potential of mean force (PMF) along each reaction coordinate, we combined metadynamics and extended-system adaptive biasing forces (meta-eABF (36, 37)) for simulations totaling 600 and 450 ns, respectively. The PMF curves, which were converged by the end of simulations (Fig. S7), illustrate that the binding free energies are approximately −7.8 kcal/mol for the Pro138 site and −10.7 kcal/mol for the Thr237 site (Fig. 6). These very favorable binding free energies further confirm the binding interface observed in the simulations of $CbpA_3^{99–268}$ and guide the mutagenesis experiments described below. We do not rule out the possibility that other portions of $CbpA_3$ that were not amenable to structural characterization in this study also bind methane clathrate or confer higher-ordered oligomers to increase the avidity of $CbpA_3^{99–268}$ to methane clathrate.

Experimental assessment of predicted interaction interface

To experimentally validate the surfaces predicted as clathrate binding, we prepared $CbpA_3^{43–283}$(P138K) and $CbpA_3^{43–283}$(T237K).

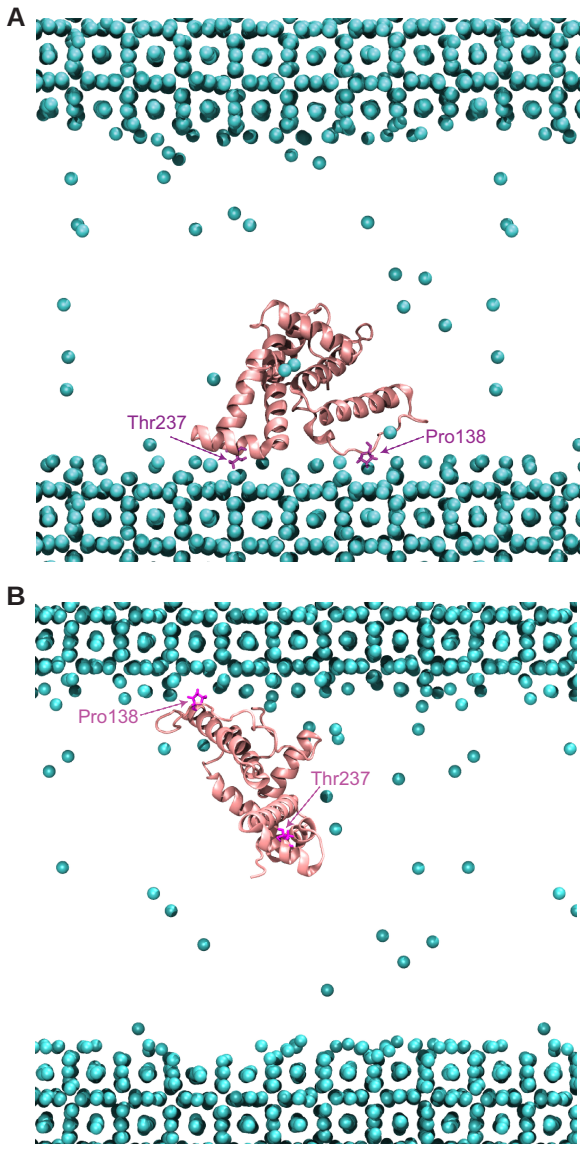

Fig. 5. MD simulations reveal spontaneous binding of $CbpA_3$ to methane clathrate. A, B) Interaction interfaces. Stable binding of $CbpA_3$ (residues 99–268, pink cartoon) to the clathrate surface in multiple orientations was observed. Methane is shown as cyan spheres; water is not shown for clarity. Residues interacting with the clathrate are highlighted in magenta on the cartoon representation. Pro138 and Thr237 are shown as magenta sticks. A) The most stable interaction through the clathrate-binding loop containing Pro138 as well as a clathrate-binding helix containing Thr237. B) Binding through the clathrate-binding loop harboring Pro138.

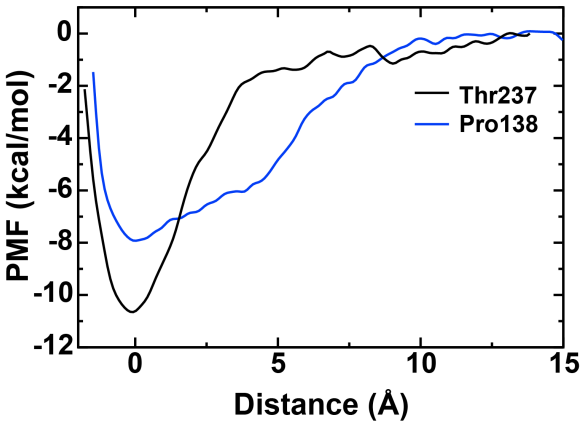

Fig. 6. PMF for separation of each binding site from the clathrate surface. The starting state for each free-energy calculation was that in Fig. 5A. A collective variable representing the distance between each respective residue (Thr237 or Pro138) and the clathrate surface was defined and used for calculating the PMF. The other side of the protein remained bound during each calculation.

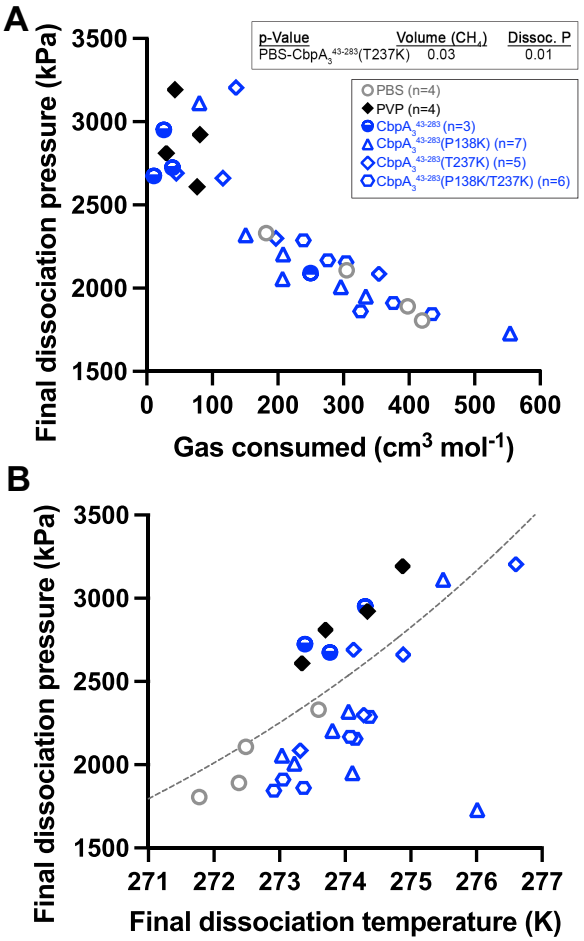

Fig. 7. Effect of $CbpA^{43–283}$ mutants on clathrate growth and stability. See Fig. 1 for details on A) and B).

Lys was selected to inhibit protein–clathrate interactions through added steric bulk and charge at the protein surface. Substitutions were made in the $CbpA_3^{43–283}$ construct, which was selected for its robust inhibition of methane clathrate (Figs. 1 and 2) and excellent expression/purification profile. $CbpA_3^{43–283}$(T237K) attenuated the inhibitory effect of $CbpA_3^{43–283}$ (Fig. 7A). $CbpA_3^{43–283}$(P138K) and a double mutant harboring both Lys mutations, $CbpA_3^{43–283}$(P138K/T237K), lost the ability to inhibit methane clathrate growth (Fig. 7A) and displayed methane clathrate stability similar to that of the buffer control (Fig. 7B). Likewise, MD simulations incorporating the Lys mutations on the $CbpA_3$ model corroborate the inactivation of the protein observed in vitro. Even with the protein starting just 4 Å from the clathrate surface in an orientation suitable for binding, it instead moved away from the surface in 100 ns simulations (Fig. S8A–C and Movies S4–S6). While the residues of the clathrate-binding surface centered on Thr237 tolerate some variability among CbpAs, Pro138 is strictly conserved

(Table S3 and Fig. S6). These data suggest that Pro138 is a key residue for clathrate binding and growth inhibition by $CbpA_3^{43–283}$. Interestingly, L-proline on its own is known to be an effective thermodynamic clathrate inhibitor (38).

Finally, to probe the role of the TxxxAxxxAxx motif, we prepared the Thr-to-Ala variant $CbpA_3^{43–283}$(T251A). Despite the conservative substitution, this construct was found exclusively in inclusion bodies, and no soluble material could be isolated. This result suggests a structural role for Thr251 integral to $CbpA_3^{43–283}$ folding. In the $CbpA_3^{99–268}$ structure, Thr251 and Thr229 side chains are within hydrogen bonding distance (Fig. 4B); this contact would be lost in $CbpA_3^{43–283}$(T251A). The Thr and Ala residues of the TxxxAxxxAxx motif are largely invariant among CbpAs (Table S3 and Fig. S6), an observation that supports the importance of these helical residues in the structural integrity of this protein family.

Discussion

Our study reveals a new protein scaffold and molecular mechanism for inhibition of gas clathrate. Bacterial $CbpA_3$, which is readily expressed and purified in preparative quantities, is a selective gas clathrate inhibitor more potent than type I AFPs and similar to PVP in both potency and resultant clathrate morphology. We found that the TxxxAxxxAxx motif in CbpA has a role in structural integrity rather than clathrate binding. A similar function was observed in the large type I AFP isoform Maxi, where the motif projects inwards in a four-helix bundle fold to help hold two dimers together by organizing internal clathrate waters (39). Despite this difference, clathrate binding occurs on two distal, flat, and largely hydrophobic protein surfaces like surfaces described for AFPs. CbpAs do not recognize ice and are selective for clathrate; this disparity is supported by the novel binding mechanism of CbpAs with methane clathrate.

While we note that the structure of $CbpA_3$ is incomplete, it largely encompasses the conserved core of CbpAs (16). The N- and C-termini may also participate in clathrate recognition and binding or could enhance interactions with clathrate surfaces through facilitating avidity; we have preliminary evidence (not shown) that CbpAs are multimeric in solution. Though we have demonstrated the structural importance of the single TxxxAxxxAxx motif in $CbpA_3$, other CbpAs harbor multiple such motifs that we have not ruled out as playing a role in clathrate binding. A full-length structure of functionally related CbpAs (16) will allow for elucidation of the role of these additional canonical motifs in gas clathrate modulation.

Bacterial CbpAs from ocean sediments hold promise for commercial application as eco-friendly substitutes for PVP and suggest that bacterial biomolecules may influence gas clathrate stability, with important repercussions for clathrate dissociation in warming oceans (40). Scaling up CbpA production as well as testing the efficacy of CbpAs on large volumes of natural gas clathrate is required before field use. Additional tests using stirred reactors (41), which mimic the environment of pipelines, as well as determining the stability of natural gas clathrates upon clathrate reformation (memory effect) in the presence of CbpAs, will inform application practicality.

The capacity for bacterial CbpAs to influence clathrate growth also lends insight into bacterial strategies for adaptation and survival in deep subsurface clathrate-containing ecosystems, which are widespread in the solar system (42). Understanding the physiological relevance of bacterial survival strategies will require additional experimentation, analogous to work done with AFPs (43–45). It remains unknown how mechanistically CbpAs might enable organismal survival in clathrate-rich environments and what concentration of protein is required to maintain a fluid niche space in gas clathrates. Answers to these questions will help elucidate the role of CbpAs in their bacterial hosts and inform technological applications.

Materials and methods

Methane clathrate growth chamber experimental design

In order to test the influence of CbpAs on methane clathrate growth, we engineered a custom pressure cell capable of generating methane clathrate from a 250-µL liquid sample droplet (46). During each experiment, the volume of methane gas consumed, which reflects the extent of clathrate growth, is obtained from measured pressure and temperature data (Fig. S9).

Recombinant protein expression and purification

CbpAs used in this study were $CbpA_2$, $CbpA_3$ and variants thereof, $CbpA_5$, and $CbpA_6$. $CbpAs_{2,3,5,6}$ were expressed and purified as previously published (16) (see Supplemental Text for details). Protein purity was confirmed by sodium dodecyl sulfate-polyacrylamide gel electrophoresis (SDS–PAGE) analysis (Fig. S10A–E), visualized with Coomassie blue staining using a ChemiDoc MP Imaging Station (Bio-Rad). Concentrations of CbpAs and variants thereof were determined using absorbance readings at 280 nm, employing extinction coefficients and molecular weights calculated with Expasy (Table S4). The concentration of $CbpA_3^{96–283}$ was estimated with a Bradford assay (Amresco), using bovine serum albumin as a calibration standard.

Methane clathrate experiments

The effect of CbpA proteins on methane clathrate growth in a pressure cell was tested following a previously established method (46) (see Supplemental Text for details). The controls were PBS (the solution in which additives were suspended), cytochrome c (Sigma-Aldrich C2506, 13 µM), PVP (Sigma-Aldrich PVP10, 13 µM), and a cocktail of type I AFPs (A/F Protein Inc., AFP type I, 13 µM).

Ice crystallization

A custom-made nanoliter osmometer (18) with a temperature stability of ±0.001°C was used to test CbpAs for ice growth inhibition (see Supplemental Text for details).

Limited proteolysis

$CbpA_3$ was subjected to limited proteolysis using the Proti-Ace and Proti-Ace 2 kits (Hampton Research). Reactions were quenched with the addition of Laemmli buffer. Proteolysis was evaluated by SDS–PAGE analysis (Figs. S3 and S11), and gels were visualized with Coomassie staining.

Identification of protein crystal constituents by mass spectrometry

Protein crystals of $CbpA_3$ were harvested and dissolved in PBS (Lonza). The resultant protein was applied to an SDS–PAGE gel, and the gel was stained with Coomassie blue for visualization (Fig. S3). Protein fragment bands were analyzed with Glu-C and Trypsin-digest mass spectrometry at the Systems Mass

Spectrometry Core at the Georgia Institute of Technology to identify the N- and C-termini of the proteolyzed $CbpA_3$.

Crystallization and structure determination of $CbpA_3$

$CbpA_3$ protein used in crystallization trials was pretreated with actinase E protease from the Proti-Ace 2 kit (Hampton Research; see Supplemental Text for details). Crystals grew within 4 months. Crystals were harvested directly from the drop and cryo-cooled in liquid nitrogen. Diffraction data were collected at the Advanced Photon Source, Argonne National Laboratories Southeast Region Collaborative Access Team (SER-CAT) beamline 22-ID. The $CbpA_3^{96–283}$ structure was deposited into PDB (ID 8DOT).

MD simulations and enhanced sampling calculations

To gain insight into potential modes of interaction of $CbpA_3$ with methane clathrate, we ran MD simulations starting from six initial protein orientations relative to a stable slab of methane clathrate surrounded by water. To estimate the binding free energies for the two binding sites identified in equilibrium simulations, we combined well-tempered metadynamics and extended-system adaptive biasing forces using the meta-eABF method (37) (see Supplemental Text for details).

Statistical analysis

Student's *t* tests were run to compare buffer-only controls with treatments. *N* and *P* values are provided in the text and figures.

Acknowledgments

The authors thank W.F. Waite for helpful discussions.

Supplementary material

Supplementary material is available at *PNAS Nexus* online.

Funding

This work was funded by a National Aeronautics and Space Administration grant (80NSSC19K0477) to J.B.G., S.D., and R.L.L.; an American Chemical Society Petroleum Research Fund grant (60191-UNI5) to R.D.; and a National Science Foundation grant (CMMI-1943722) to S.D. Synchrotron data were collected at Southeast Regional Collaborative Access Team (SER-CAT) 22-ID (beamline at the Advanced Photon Source, Argonne National Laboratory). SER-CAT is supported by its member institutions and equipment grants (S10_RR25528, S10_RR028976, and S10_OD 027000) from the National Institutes of Health. Computational resources were provided through XSEDE (TG-MCB130173), which is supported by the US National Science Foundation (NSF; ACI-1548562). This work also used the Hive cluster, which is supported by the NSF (MRI-1828187) and is managed by PACE at Georgia Tech. A.M.J. received support from a Georgia Institute of Technology Ocean Science and Engineering PhD Fellowship and a PEO Scholar Award. L.G.K. was supported through participation in a Beckman Scholars Program award received from the Arnold and Mabel Beckman Foundation. M.X. received support from a Georgia Institute of Technology President's Undergraduate Research Award.

Author contributions

Conceptualization: D.J.E.H., A.M.J., J.C.G., S.D., R.L.L., J.B.G.; Methodology: D.J.E.H., A.M.J., Z.F., R.D., J.C.G., S.D., R.L.L., J.B.G.; Investigation: D.J.E.H., A.M.J., Z.F., L.G.K., M.X., R.D.; Visualization: D.J.E.H., A.M.J., Z.F., J.C.G., J.B.G.; Supervision: J.C.G., S.D., R.L.L., J.B.G.; Writing—original draft: D.J.E.H., A.M.J., R.L.L., J.B.G.; Writing—review and editing: D.J.E.H., A.M.J., Z.F., L.G.K., M.X., R.D., J.C.G., S.D., R.L.L., J.B.G.

Data availability

The $CbpA_3^{96–283}$ structure is available at PDB (ID 8DOT). All other data are included in the manuscript and/or supporting material.

References

1 Davie MK, Buffett BA. 2003. Sources of methane for marine gas hydrate: inferences from a comparison of observations and numerical models. *Earth Planet Sci Lett*. 206:51–63.
2 Malinverno A. 2010. Marine gas hydrates in thin sand layers that soak up microbial methane. *Earth Planet Sci Lett*. 292(3–4):399–408.
3 Wallmann K, *et al.* 2012. The global inventory of methane hydrate in marine sediments: a theoretical approach. *Energies*. 5(12):2449–2498.
4 Boswell R, Collett TS. 2011. Current perspectives on gas hydrate resources. *Energy Environ Sci*. 4(4):1206–1215.
5 Glass JB, Dierssen HM, Glein CR, Schmidt BE, Winebrenner DP. 2022. Defining and characterizing habitable environments in ocean world systems. *Oceanography*. 35(1):30–38.
6 Glass JB, *et al.* 2021. Microbial metabolism and adaptations in Atribacteria-dominated methane hydrate sediments. *Environ Microbiol*. 23(8):4646–4660.
7 McConnell DR, Zhang Z, Boswell R. 2012. Review of progress in evaluating gas hydrate drilling hazards. *Mar Pet Geol*. 34(1):209–223.
8 Gao Y, *et al.* 2018. Risk analysis on the blowout in deepwater drilling when encountering hydrate-bearing reservoir. *Ocean Eng*. 170:1–5.
9 Khan MS, Lal B, Bustam MA. 2020. Gas hydrate inhibitors. In: Lal B, Nashed O, editors. *Chemical additives for gas hydrates*. Cham: Springer. p. 27–46.
10 Nasir Q, Suleman H, Elsheikh YA. 2020. A review on the role and impact of various additives as promoters/inhibitors for gas hydrate formation. *J Nat Gas Sci Eng*. 76:103211.
11 Kaiser MJ. 2019. Activity-based costing. In: Kaiser MJ, editor. *Decommissioning forecasting and operating cost estimation*. Houston (TX): Gulf Professional Publishing. p. 489–522.
12 Ke W, Kelland MA. 2016. Kinetic hydrate inhibitor studies for gas hydrate systems: a review of experimental equipment and test methods. *Energy Fuels*. 30(12):10015–10028.
13 Julinová M, Vaňharová L, Jurča M. 2018. Water-soluble polymeric xenobiotics—polyvinyl alcohol and polyvinylpyrrolidon—and potential solutions to environmental issues: a brief review. *J Environ Manage*. 228:213–222.
14 Walker VK, *et al.* 2015. Antifreeze proteins as gas hydrate inhibitors. *Can J Chem*. 93(8):839–849.
15 Udegbunam LU, DuQuesnay JR, Osorio L, Walker VK, Beltran JG. 2018. Phase equilibria, kinetics and morphology of methane hydrate inhibited by antifreeze proteins: application of a novel 3-in-1 method. *J Chem Thermodyn*. 117:155–163.
16 Johnson AM, *et al.* 2020. Mainly on the plane: deep subsurface bacterial proteins bind and alter clathrate structure. *Cryst Growth Des*. 20(10):6290–6295.

17 Sloan ED Jr, Koh CA. 2007. *Clathrate hydrates of natural gases*. 3rd ed. Boca Raton (FL): CRC Press.
18 Berger T, *et al.* 2019. Synergy between antifreeze proteins is driven by complementary ice-binding. *J Am Chem Soc*. 141(48): 19144–19150.
19 Basu K, *et al.* 2014. Determining the ice-binding planes of antifreeze proteins by fluorescence-based ice plane affinity. *J Vis Exp*. 83:e51185.
20 Al-Adel S, Dick JAG, El-Ghafari R, Servio P. 2008. The effect of biological and polymeric inhibitors on methane gas hydrate growth kinetics. *Fluid Ph Equilibria*. 267(1):92–98.
21 Daraboina N, Linga P, Ripmeester J, Walker VK, Englezos P. 2011. Natural gas hydrate formation and decomposition in the presence of kinetic inhibitors. 2. Stirred reactor experiments. *Energ Fuel*. 25(10):4384–4391.
22 Daraboina N, Moudrakovski IL, Ripmeester JA, Walker VK, Englezos P. 2013. Assessing the performance of commercial and biological gas hydrate inhibitors using nuclear magnetic resonance microscopy and a stirred autoclave. *Fuel*. 105:630–635.
23 Sharifi H, Walker VK, Ripmeester J, Englezos P. 2014. Insights into the behavior of biological clathrate hydrate inhibitors in aqueous saline solutions. *Cryst Growth Des*. 14(6):2923–2930.
24 Zeng H, Wilson LD, Walker VK, Ripmeester JA. 2003. The inhibition of tetrahydrofuran clathrate-hydrate formation with antifreeze protein. *Can J Phys*. 81(1–2):17–24.
25 Zeng H, Moudrakovski IL, Ripmeester JA, Walker VK. 2006. Effect of antifreeze protein on nucleation, growth and memory of gas hydrates. *AIChE J*. 52(9):3304–3309.
26 Ohno H, Susilo R, Gordienko R, Ripmeester J, Walker VK. 2010. Interaction of antifreeze proteins with hydrocarbon hydrates. *Chem Eur J*. 16(34):10409–10417.
27 Gordienko R, *et al.* 2010. Towards a green hydrate inhibitor: imaging antifreeze proteins on clathrates. *PLoS One*. 5(2):e8953.
28 Myran D, Middleton A, Choi J, Gordienko R, Ohno H, Ripmeester JA, Walker VK. 2011. Genetically-engineered mutant antifreeze proteins provide insight into hydrate inhibition. Proceedings of the 7th International Conference on Gas Hydrates. 17–21 July 2011, Edinburgh, UK.
29 Chen X, Espinoza DN. 2018. Ostwald ripening changes the pore habit and spatial variability of clathrate hydrate. *Fuel*. 214: 614–622.
30 Jung JW, Espinoza DN, Santamarina JC. 2010. Properties and phenomena relevant to CH_4-CO_2 replacement in hydrate-bearing sediments. *J Geophys Res*. 115:B10.
31 Servio P, Englezos P. 2003. Morphology of methane and carbon dioxide hydrates formed from water droplets. *AIChE J*. 49(1): 269–276.
32 Bruusgaard H, Lessard LD, Servio P. 2009. Morphology study of structure I methane hydrate formation and decomposition of water droplets in the presence of biological and polymeric kinetic inhibitors. *Cryst Growth Des*. 9(7):3014–3023.
33 Jumper J, *et al.* 2021. Highly accurate protein structure prediction with AlphaFold. *Nature*. 596(7873):583–589.
34 Mirdita M, *et al.* 2022. Colabfold: making protein folding accessible to all. *Nat Methods*. 19:679–682.
35 Bagherzadeh SA, Alavi S, Ripmeester JA, Englezos P. 2015. Why ice-binding type I antifreeze protein acts as a gas hydrate crystal inhibitor. *Phys Chem Chem Phys*. 17(15):9984–9990.
36 Fiorin G, Klein ML, Hénin J. 2013. Using collective variables to drive molecular dynamics simulations. *Mol Phys*. 111(22–23): 3345–3362.
37 Fu H, *et al.* 2018. Zooming across the free-energy landscape: shaving barriers, and flooding valleys. *J Phys Chem*. 9(16):4738–4745.
38 Sa J-H, *et al.* 2016. Inhibition of methane and natural gas hydrate formation by altering the structure of water with amino acids. *Sci Rep*. 6(1):1–9.
39 Sun T, Lin FH, Campbell RL, Allingham JS, Davies PL. 2014. An antifreeze protein folds with an interior network of more than 400 semi-clathrate waters. *Science*. 343(6172):795–798.
40 Glass JB. 2023. What is the role of microbes in gas hydrate formation and stability? *Environ Microbiol*. 25(1):45–48.
41 Ke W, Kelland MA. 2016. Kinetic hydrate inhibitor studies for gas hydrate systems: a review of experimental equipment and test methods. *Energ Fuels*. 30(12):10015–10028.
42 Mousis O, *et al.* 2015. Methane clathrates in the solar system. *Astrobiology*. 15(4):308–326.
43 Chakraborty S, Jana B. 2018. An unusual tale of structural evolution, hydration and function. *Proc Indian Natl Sci Acad* 1:169–187.
44 Davies PL. 2014. Ice-binding proteins: a remarkable diversity of structures for stopping and starting ice growth. *Trends Biochem Sci*. 39(11):548–555.
45 Bar Dolev M, Braslavsky I, Davies PL. 2016. Ice-binding proteins and their function. *Annu Rev Biochem*. 85:515–542.
46 Johnson AM, Zhao Y, Kim J, Dai S, Glass JB. 2021. Methane hydrate crystallization on sessile water droplets. *J Vis Exp*. 171: e62686.